Nanoscale

Accepted Manuscript

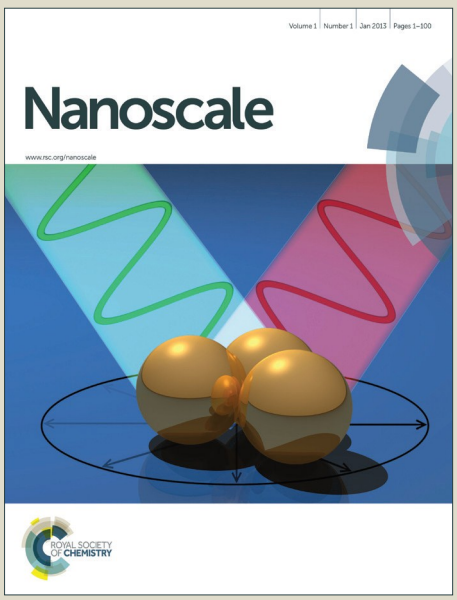

ROYAL SOCIETY OF CHEMISTRY

www.rsc.org/nanoscale

Cite this: DOI: 10.1039/c0xx00000x

www.rsc.org/xxxxxx

ARTICLE TYPE

Monoatomic-thick Graphitic Carbon Nitride Dots on Graphene Sheets as An Efficient Catalyst in Oxygen Reduction Reaction

Xiaopeng Wang,[a] Lixia Wang,[a] Fei Zhao,[a] Chuangang Hu,[a] Yang Zhao,[a] Zhipan Zhang,*[a] Shilu Chen,*[a] Gaoquan Shi[b] and Liangti Qu*[a]

Received (in XXX, XXX) Xth XXXXXXXXX 20XX, Accepted Xth XXXXXXXXX 20XX
DOI: 10.1039/b000000x

Atomically thick two-dimensional materials have been increasingly attracting research interests not only due to their promising applications in a range of functional devices but also their theoretical values to unravel the catalytic electron transfer process within a simplified scenario. In this work, the monoatomic-thick dot-sized graphitic carbon nitride (g-C_3N_4) has been synthesized and intimately contacted to the basal plane of the graphene sheet to form the monolayer g-C_3N_4 dots@graphene (MTCG). The electrocatalytic activity of the MTCG in the oxygen reduction reaction is found to rival that of the commercial Pt/C catalyst in terms of the catalytic current density and half-wave potential. The density functional theory calculations confirm the catalytic improvement of the MTCG originates from a higher efficiency for the reduction of OOH^- than the g-C_3N_4 alone, therefore the current work is expected to provide new insights in developing next generation, highly-efficient catalysts for the oxygen reduction reaction.

1. Introduction

Two-dimensional (2D) ultrathin materials with atomic or molecular layer thickness have attracted tremendous attention because of their fascinating nature associated with high percentage of exposed surface atoms compared to their bulk counterparts in broad application prospects.[1, 2] Generally, the 2D ultrathin sheets feature with a vast number of active edge sites that are preferentially desirable in heterogeneous catalysis as they could potentially serve as efficient catalytic centers with high catalytic activity. For instance, 2D atomic-thick ZnSe sheets with surface distortions had enhanced photoconversion efficiency and photostability, showing two orders of magnitude higher solar water splitting activity compared to the their bulk counterparts.[3] SnS_2 single-layers possessed higher carrier mobility than bulk SnS_2 materials and led to a notable enhancement in visible-light water-splitting properties,[4] while ultrathin SnO_2 sheets with abundant four-coordinate surface Sn atoms favored CO adsorption and demonstrated remarkable improvement in CO catalytic performances over thicker SnO_2 sheets.[5] At the same time, the atomic-thick 2D materials additionally render a rare opportunity to rationalize the mechanistic pathways of the catalytic reaction by resorting to theoretical models with less atoms and thus higher accuracies than those of the bulk materials, eventually leading to an atomic-level insight into the process of the catalysis reaction to study the mutual relationship between the structure of materials and their corresponding properties.[6]

Among various investigated 2D materials, graphitic carbon nitride (g-C_3N_4) with a delocalized π-conjugated structure has emerged as new class of interesting graphene derivatives with a medium-bandgap and worked effectively in hydrogen storage, bioimaging and catalytic water splitting reactions.[7–9] Apart from the aforementioned applications, g-C_3N_4 has recently been identified as a promising metal-free electrocatalyst for some basic but important electrochemical reactions such as the hydrogen evolution reaction (HER), oxygen evolution reaction (OER) and oxygen reduction reaction (ORR), which are crucial steps in various clean energy conversion and storage systems in the fields of photoelectrochemical cells, fuel cells and lithium-air batteries.[10–14] Despite that g-C_3N_4 has shown impressive catalytic activities in HER and ORR, its low intrinsic electrical conductivity significantly limits its performance and further improvements. In addition, compared to the easy exfoliation of graphite into monolayer/few-layer graphene flakes due to the weak Van der Waals interaction between graphitic layers, it is exceptionally difficult to exfoliate bulk g-C_3N_4 prepared from thermal condensation of organic precursors into monodispersed atomic-thick g-C_3N_4 sheets because the strong hydrogen bondings between polymeric melon units with NH/NH_2 groups in neighboring layers are considerably less vulnerable to acidic/thermal exfoliations.[15,16] Consequently, the synthesis of atomic-thick g-C_3N_4 with high electrocatalytic activity in ORR is still in its infancy and the exact catalytic mechanism of ultrathin g-C_3N_4 in ORR remains even more elusive.[17]

As a perfect "flatland", graphene is a 2D monoatomic-thick sheet of carbon atoms arranged in the honeycomb pattern with an excellent conductivity in heat and electricity, as well as many other intriguing features such as high chemical/thermal stability and superior mechanical flexibility.[18] Considering the outstanding electrical conductivity of graphene and the structural similarity

between g-C_3N_4 and graphene, it is natural to introduce the graphene component into the g-C_3N_4 system to ameliorate the poor conductivity of g-C_3N_4 and enhance its electrocatalytic activity in the ORR. For example, Müllen and co-workers reported sandwich-like graphene/ g-C_3N_4 composite by using nanocasting technology,[13] while Sun and co-workers prepared three-dimensional (3D) graphene/g-C_3N_4 hybrid by photoreduction method.[19] Unfortunately, previous attempts to enhance the electrocatalytic activity of g-$C_3N_4$by combining g-C_3N_4 and graphene show little sign of synergistic coupling interaction between g-C_3N_4 and graphene, producing catalysts inferior to the widely used commercial Pt-based catalysts yet without a systematic mechanistic study on the ORR process.

In this work, we have successfully prepared the monoatomic-thick g-C_3N_4 dots (MTCs) by an oxidative exfoliation and achieved a face-to-face g-C_3N_4/graphene basal plane contact to form the MTC@graphene (MTCG) through self-assembling under a hydrothermal condition. The MTCG system apparently possesses a series of advantages over the conventional g-C_3N_4 or simple mixtures of g-C_3N_4/graphene catalysts in the ORR. On one hand, the MTC component benefits from the high exposure of surface atoms that function as the active catalytic sites in the ORR and the intimate contact between g-C_3N_4 and graphene basal plane ensures a facile electron flow at the g-C_3N_4/graphene interface, thus eliminating the bottleneck of electron transport through different g-C_3N_4 layers within the highly resistive multilayer g-C_3N_4 materials. On the other hand, the graphene support serves as the conductive footstone for the MTC and forms an interconnected 3D framework that connects all catalytic sites with fast electron transport and ample microporous/macroporous channels facilitating the diffusion of guest molecules and electrolytes in the ORR. Indeed, the MTCG is found to have an excellent electrocatalytic activity rivaling that of the commercial Pt/C catalyst in the ORR and the density functional theory (DFT) calculations confirm the existence of a synergistic coupling interaction between g-C_3N_4 and graphene that accounts for the notable improvement in the catalytic performance. More importantly, since the prepared MTC can be reasonably approximated as an ensemble of only a few tens of C and N atoms in a confined dimension, the current work also provides one rare opportunity to verify the proposed mechanism of g-C_3N_4-catalyzed ORR by DFT calculations based on models with high accuracies and thus less deviations from what takes place in reality at the g-C_3N_4 catalytic sites during the ORR. To the best of our knowledge, the MTCG shows the highest electrocatalytic activities for g-C_3N_4-based catalysts in the ORR under alkaline solution conditions till now and the current work represents the first effort to rationalize the mechanism of g-C_3N_4-catalyzed ORR with an accurate model commensurate with the actual dimension of the g-C_3N_4 material and the experimental results as well.

2. Experiment

2.1 Synthesis of the graphene oxide (GO) and monoatomic-thick g-C_3N_4 dots (MTC)

GO was prepared from natural graphite powder *via* acid-oxidation according to modified Hummers method as mentioned in our previous papers.[20–22] Bulk g-C_3N_4 was prepared by heating melamine for 4 h to 550 ℃ and kept at this temperature for another 4 h in air. MTC was prepared by modified Hummers method in the following process. The as-prepared bulk g-C_3N_4 (5 g) and sodium nitrate (1 g) were firstly mixed with 100 mL of H_2SO_4 (98 wt %) in a 200 mL flask and stirred for 1 day at room temperature. A "chain-like" g-C_3N_4 (denoted as CLC) structure was resolved at this step. Then potassium permanganate (7 g) was added to the suspension for 4 h at room temperature. Subsequently, the suspension was poured to 200 mL of ice-water mixture with 20 mL hydrogen peroxide under a slow stirring, with the color changing from brown to white. Then the suspension was centrifuged to 20 min at about 8000 rpm to remove the residual unexfoliated component. After, the supernatant was ultrasonicated for 1h and the remaining salt impurities were removed by dialysis. Finally the supernatant was filtered using double layer filter membrane with the pores size of 220 nm to extract MTC.

2.2 Preparation of the monoatomic-thick g-C_3N_4 dots@graphene (MTCG) catalyst

Aqueous solutions of the MTC (1.5 mg mL^{-1}, 20 mL) and GO (4 mg mL^{-1}, 20mL) were mixed together and transferred into a 50 mL Teflon-line stainless-steel autoclave before heated at 220 ℃ for 3 h. A hydrogel sample was then obtained and the lyophilization was applied to prevent the aggregation of graphene sheets during drying process. A control sample of CLC@graphene was synthesized by following the same procedure except that CLC was used instead of MTC as the starting material.

2.3 Preparation of the reduced graphene oxide (G)

In order to clearly show the characteristics of the structure and electrochemical activity of the MTC and MTCG, a control sample of reduced graphene oxide (G) without the MTC was synthesized under the same hydrothermal process. A solution of GO (4 mg mL^{-1}, 20 mL) was mixed with deionized water (20 ml) and transferred into a 50 mL Teflon-line stainless-steel autoclave before heated at 220 ^oC for 3 h. Then, the obtained hydrogel sample was dried by the lyophilization technology to give G.

2.4 Characterization

The morphology of the samples was determined by scanning (SEM, JSM-7500F) and transmission electron microscopy (TEM, JEM, 2100). The elemental mappings were carried out on a scanning transmission electron microscope (STEM) unit with high-angle annular dark-field (HAADF) detector (HITACHI S-5500) operating at 30 kV. X-ray diffraction (XRD) patterns were obtained by using a Netherlands 1,710 diffractometer with a Cu Kα irradiation source (λ = 1.54 Å). Fourier transformed infrared (FTIR) spectra were recorded on a Bruker VERTEX 700 spectrometer between 3500 and 600 cm^{-1}. X-ray photoelectron spectroscopy (XPS) data were obtained with an ESCALab220i-XL electron spectrometer from VG Scientific using 300W Al Kα radiation. The base pressure was about 3×10^{-9} mbar. The binding energies were referenced to the C1s line at 284.8 eV from adventitious carbon. Thermogravimetric analysis (TGA) was conducted on the TGA/DTA1 STAR system, Metter Toledo. The samples were put in a 70 μL crucible with a programmed heating rate of 10 °C/min from 25 to 1000 °C under nitrogen atmosphere.

The optical absorption spectra were collected on a UV-visible spectrophotometer (Shimadzu, Japan). Fluorescent emission spectra were recorded on a RF-5301PC spectrofluorometer (Shimadzu, Japan).

2.5 Electrochemical measurement

Prior to use, the working electrode is polished mechanically and washed with Milli-Q water and acetone before naturally dried. Then, 0.5 mg MTCG is dissolved in 1 mL solvent mixture of Nafion (5% aqueous solution) and EtOH (V: V ratio = 1:9) by sonication. 0.4 μL MTCG suspension is pipetted on the glassy carbon electrode surface and the electrode is allowed to dry at 50 ^{o}C for 1 h before measurement. A Pt wire (0.5 mm in diameter) and an Ag/AgCl electrode were used as the counter and reference electrodes, respectively. Control experiments with the MTC and commercial Pt/C catalysts (20 wt% platinum on carbon black) of the same amount were also studied for comparison. N_2 or O_2 purging was used to give the O_2-free or O_2-saturated electrolyte solution. The cyclic voltammetry tests of the MTC, MTCG and commercial Pt/C catalyst were performed in an O_2-saturated 0.1 M KOH in the potential range from -0.8 to 0.2 V at a scan rate of 10 mV s^{-1}. Measurements on the rotating ring-disk electrode (RRDE) were carried out on a MSRX electrode rotator (Pine Instrument) and the CHI 760D potentiostat at a scan rate of 10 mV s^{-1}.

3. Results and discussion

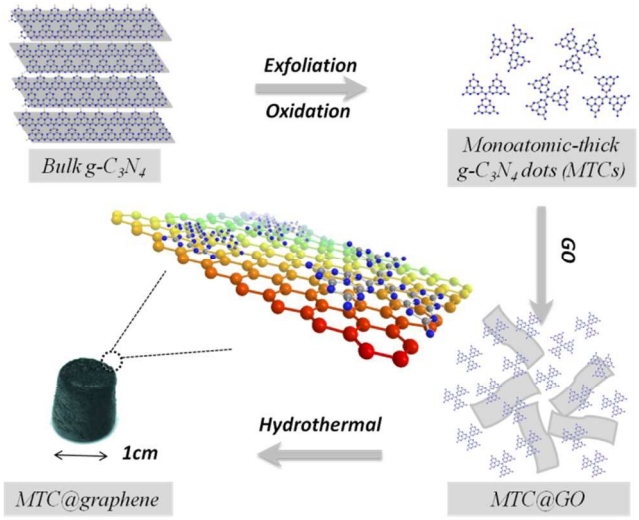

Scheme 1. Proposed synthetic protocol for the monoatomic-thick g-C_3N_4 dots@graphene (MTCG).

Scheme 1 summarizes the preparation of the MTCG. The MTC was first oxidatively exfoliated from the bulk g-C_3N_4 by a modified Hummers method and then mixed with graphene oxide (GO) to form an intimate contact onto graphene surfaces through the synergic effects of the π-π interaction and structural resemblance. The MTCG catalyst was then obtained by self-assembling GO hydrothermally. In the hydrothermal process, GO sheets were also reduced due to the high temperature. In order to clearly show the structural and catalytic characteristics of the MTCG, control sample of reduced graphene oxide (G) was synthesized by hydrothermally treating GO in the absence of the MTC under the same hydrothermal process. Details of the experimental procedures can be found in the Methods section. After the intercalation of H_2SO_4 and sodium nitrate in the interlayer space of g-C_3N_4, the bulk g-C_3N_4 was exfoliated into thinner g-C_3N_4 as shown by the TEM image in Fig. S1. Compared to the bulk g-C_3N_4, the "chain-like" structure and the transparent feature of this intermediate suggests that the original 2D planar structure of bulk g-C_3N_4 was cut into smaller pieces concomitant with delamination of thick g-C_3N_4 layers during the H_2SO_4 etching process of bulk g-C_3N_4 into thinner g-C_3N_4 sheets. Finally, large scale MTC can be obtained with the extended reaction time and the addition of potassium permanganate, where the "chain-like" g-C_3N_4 (denoted as CLC) was further etched by potassium permanganate to form MTC dots. The morphology of the MTC was first characterized with TEM and atomic force microscope (AFM). The TEM and AFM images in Fig. S2 show that the MTC has a monoatomic thickness of around 0.4 nm and a diameter of 31 nm. Meanwhile, the GO sheets exhibit an average size of *ca*. 3 μm in the AFM images (Fig. S3), therefore providing a flat surface large enough to host the nano-sized MTC in a face-to-face manner.

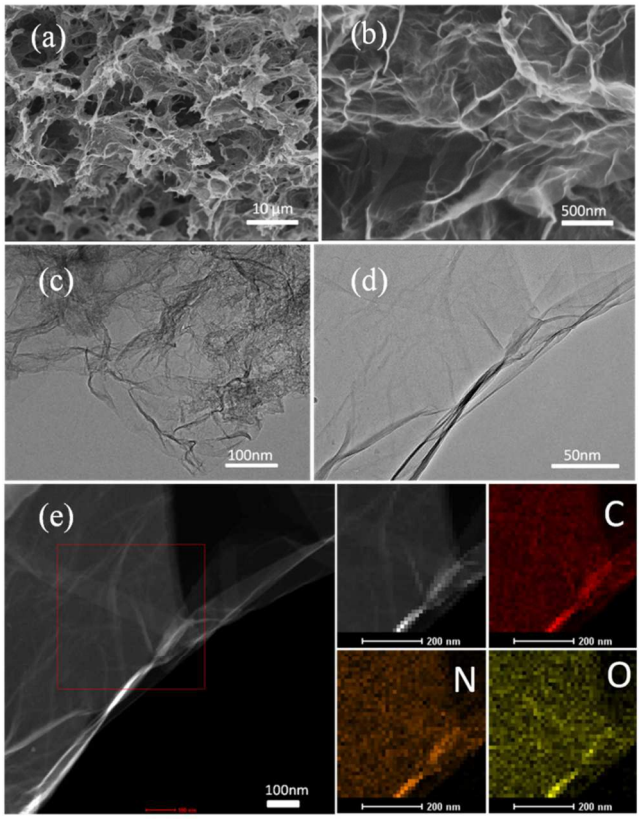

Fig. 1 Typical (a,b) SEM, (c,d) TEM and (e) STEM images at different magnifications of the MTCG catalyst with elemental mapping images of C, N and O elements, respectively.

Scanning electron microscopy (SEM) and TEM were employed to characterize the structure of the MTCG catalyst. A well-defined and interconnected 3D porous architecture can be clearly observed in Fig. 1a and 1b, forming a conductive network that would facilitate the charge transport in the ORR process. As the g-C_3N_4 dots on the graphene basal plane is only monoatomically thick, it is not conspicuous in the TEM images (Fig. 1c and 1d). However, scanning transmission electron

microscopy (STEM) elemental mappings (Fig. 1e) reveal a uniform distribution of C and N elements throughout the material, suggesting the homogeneous presence of g-C_3N_4 on the graphene surface. The presence of g-C_3N_4 in the MTCG manifests itself as the broadened peak from 20° to 30° in the XRD pattern (Fig. S4), implying the existence of π-π stacking between the g-C_3N_4 and graphene sheets, as is also reflected in the characteristic set of Raman peaks between ca. 1700 and 800 cm^{-1} originated from s-triazine derivatives in the Fourier transform infrared (FTIR) spectra (Fig. S5).[23] Meanwhile, the dominant absorption peak of the MTC at ~230 nm is red-shifted to ~280 nm for the MTCG in the UV-Vis absorption spectra (Fig. S6) and the strong fluorescence of the MTC in the photoluminescence (PL) spectrum vanish in the MTCG (Fig. S7), indicating that the g-C_3N_4 resides intimately on the graphene sheet and therefore the excited state of g-C_3N_4 can effectively be quenched by the underlying graphene.[19] In addition, the thermogravimetric analysis (TGA) (Fig. S8) of the MTCG showed a weight loss of approximately 22% between 500 and 700 °C under a nitrogen flow, corresponding to the decomposition of g-C_3N_4. Hence the g-C_3N_4 content in the MTCG sample was determined to be approximately 22wt%, close to the theoretical g-C_3N_4 loading of 27wt% in the current experimental conditions.

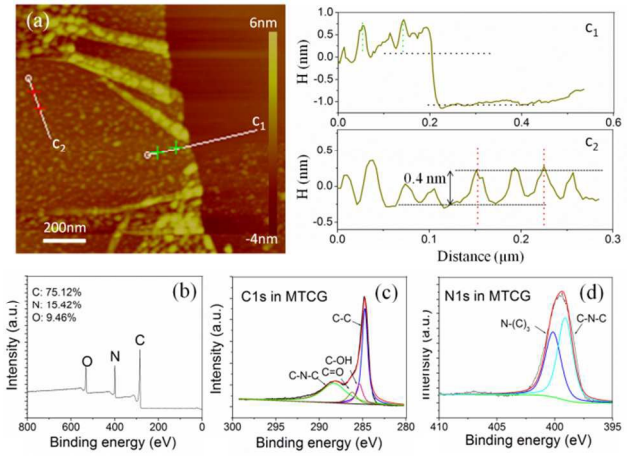

Fig. 2 (a) The AFM image and corresponding height analyses along the lines marked in the AFM image (c1-c2) of the MTCG. XPS spectra (b) survey, (c) C1s and (d) N1s of the MTCG.

More importantly, the layered structure of the MTCG is probed by the AFM topological measurement displayed in Fig. 2, enabling a direct analysis on the thickness of the MTC and the underlying graphene sheet. As plotted in the right panel of Fig. 2a, the heights of g-C_3N_4 and graphene sheet are found to be in the range of *ca*. 0.4 nm and 1 nm, respectively, verifying that the g-C_3N_4 dots anchored on the graphene surface in the form of monolayer. To further investigate the chemical composition of the MTCG, the XPS measurements were preformed. The XPS survey spectrum (Fig. 2b) of the MTCG catalyst shows the presence of C1s, O1s, and N1s without any other impurities, as is also observed in that of the MTC (Fig. S9). The inset specifies the atomic percentage of the elements and the calculated N/C atomic ratio is about 20%. The high resolution C1s spectra in Fig. 2c were deconvoluted into four different peaks centering at 284.6 eV, 285.3 eV, 286.2 eV and 288.0 eV, while the C1 peak at 288 eV and 284.6 eV is the main contribution. The 288 eV peak is assigned to sp2 C atoms in the triazine rings attached to N inside the aromatic structure group or -NH_2 group as originating from g-C_3N_4.[23] The 284.6 eV peak is typically assigned to graphitic carbon in the literature originating from graphene. The 285.3 eV, 286.2 eV peak are typically corresponding to C-OH group and C=O group.[24–26] The high resolution N1s spectra can be separated into two peaks for s-triazine rings (C-N-C, 398.8 eV) and bridging N atoms in N-$(C)_3$ (400.1 eV).[23,27] All these characterizations unambiguously confirm the formation of monolayer g-C_3N_4 homogeneously on the interconnected 3D graphene networks.

To study the ORR catalytic activity, the MTCG was loaded onto the glassy carbon electrode and first evaluated by cyclic voltammetry (CV) measurements in a three-electrode system with the 0.1 M KOH solution as the electrolyte. For comparison, the MTC and commercial Pt/C (20 wt%) catalyst were also measured in the same condition. As shown in Fig. 3a, when the working electrode was loaded with 0.08 mg cm^{-2} MTCG catalyst and the electrolyte was saturated with O_2, a pronounced cathodic peak of the electrocatalytic reduction of oxygen can be well resolved at -0.13 V *vs*. Ag/AgCl reference electrode, which is very close to the peak potential of the Pt/C catalyst. In comparison, the MTC only shows a broad reduction peak at around -0.46 V vs. Ag/AgCl with a much smaller current density (Fig. S10). The remarkable ORR activity of the MTCG catalyst is also reflected by its early onset potential (E_{on} = -20 mV) and half-wave potential ($E_{1/2}$ = -90 ± 1 mV) measured by the rotating ring-disk electrode (RRDE) polarization curves (Fig. 3b). As a reference, though the onset potential (E_{on} = 30 mV) of the Pt/C catalyst is slightly more positive than that of the MTCG catalyst, its catalytic current density is considerably smaller than that of the MTCG, featuring an even more negative half-wave potential ($E_{1/2}$ = -105 ± 1 mV). Therefore, the MTCG catalyst is a far superior ORR catalyst to the MTC in terms of onset potential, half-wave potential and the catalytic ORR limiting current density, validating the beneficial effects of graphene-mediation in improving the catalytic performance of the MTC in the ORR. To rule out any possible significant oxygen reduction catalyzed by the graphene component in the MTCG, the electrocatalytic activity of the control sample of reduced graphene oxide (G) was also measured in the O_2-saturated 0.1 M KOH aqueous solution. As demonstrated in Fig. S11, the G merely shows a negligible ORR current density compared to the MTCG, implying that the observed well-improved ORR activity of the MTCG over that of the MTC should originate from a synergistic effect between the MTC and G rather than a simple conductivity improvement induced by the incorporation of the G component. Interestingly, when the larger-sized and multilayered CLC was attached on graphene by following the same hydrothermal preparation of MTC to MTCG, the ORR performance of CLC@graphene is still inferior to that of the MTCG (Fig. S12), demonstrating the importance of a homogeneous and intimate contact between individual g-C_3N_4 and graphene layers on the ORR properties of the MTCG. Moreover, to verify the influence of oxygenated groups in the ORR, MTCG was further reduced by hydrazine vapor to remove oxygenated functional groups. The energy dispersive spectroscopy (EDS) shows a tiny feature of oxygen content after the hydrazine vapor treatment (Fig. S13b), while the

ORR catalytic activity of hydrazine reduced MTCG highly resembles that of the original MTCG (Fig. S13c), suggesting the oxygenated groups in the MTCG has a very small (if any) influence on the catalytic activity in the ORR. The oxygen content originates from the oxidative exfoliation preparation of the MTC, as the XPS spectra of the MTC confirm the oxygen content (Fig. S9b) and the presence of C=O and C-OH bonds (Fig. S9c). Therefore, the barely changed catalytic ORR performance of the MTCG samples with varied oxygen content shown in Fig. S13 reveals that the oxygenated groups in the MTCG either do not take part in the ORR or have very little effect on the rate limiting step of electron transfer from catalysts to free OOH^- during the reduction of free OOH^- in the ORR as proposed by our theoretical model in Fig. 4 (*vide infra*).

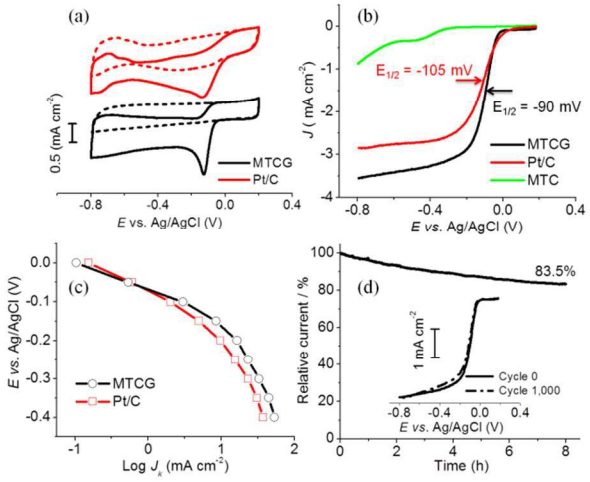

Fig. 3 (a) Cyclic voltammetry (CV) curves of the MTCG and Pt/C catalysts at a scan rate of 10 mV s^{-1} in the O_2-saturated (solid lines) or N_2-saturated (dash lines) 0.1 M KOH solution. (b) RRDE polarization curves of the MTC, MTCG and Pt/C catalysts with a scan rate of 10 mV s^{-1} at 1,200 rpm in the O_2-saturated 0.1 M KOH solution. The arrows indicate the position of the half-wave potential ($E_{1/2}$). (c) Tafel plots obtained from the RRDE measurements on the MTCG and Pt/C at 1,200 rpm. (d) Chronoamperometric responses of the MTCG for 8 h at -0.3V in an O_2-saturated 0.1 M KOH at 1,200 rpm, the inset shows RRDE curves of the MTCG catalyst at Cycle 0 (solid line) and Cycle 1,000 (dash line) when the catalysts were cycled between -0.8 and 0.2 V with a scan rate of 10 mV s^{-1} at 1,200 rpm in the O_2-saturated solution, manifesting a negligible negative shift in the $E_{1/2}$.

Additionally, the overall kinetics of the MTCG and Pt/C catalysts in the ORR process were further scrutinized by their Tafel plots extrapolated from the linear sweep voltammograms (LSVs) at 1,200 rpm according to Equation S1. As shown in Fig. 3c, both plots display a distinct two-stage feature, with a smaller slope in the low overpotential region (for E > -0.15 V vs. Ag/AgCl) where the ORR is limited by the surface reaction rate on the catalyst and a much steeper curve observed at higher overpotentials where the ORR catalytic activity is more dependent on the oxygen diffusion. [11, 28] The Tafel slopes of the MTCG are calculated as 59 mV and 240 mV per decade in the low overpotential and high overpotential regions, respectively. These values are comparable to those of the Pt/C catalyst (65 mV and 210 mV per decade, respectively) in the corresponding regions, implying the MTCG could effectively catalyze the ORR as facilely as the Pt/C does. As listed in Table 1, the current results of the MTCG in the electrochemical measurements unambiguously entitles the MTCG to be the most efficient g-C_3N_4-based ORR catalysts reported so far in terms of the peak potential, onset potential and half-wave potential.

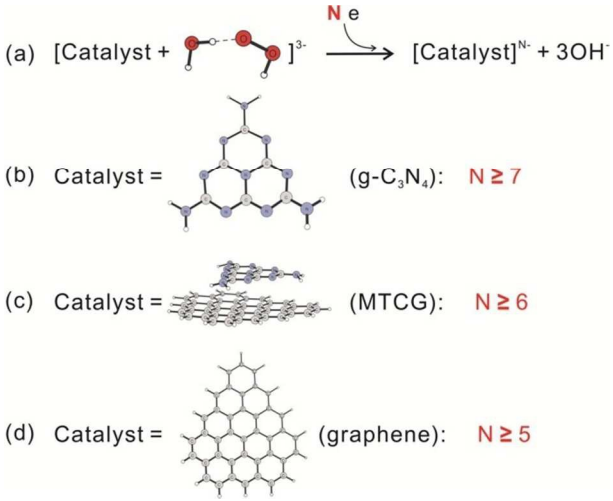

Fig. 4 (a) The number of additional electrons required by the decomposition of the H_2O-OOH^- complex into three hydroxides when catalyzed by (b) the g-C_3N_4, (c) MTCG and d) graphene, respectively.

The durability of the MTCG and Pt/C catalysts were evaluated by cycling the catalysts in the potential range of -0.8 to 0.2 V at a scan rate of 10 mV s^{-1} in the O_2-saturated solution.[31,32] For the MTCG, there is no performance loss after 1,000 cycles except a negligible negative shift in the $E_{1/2}$ value of 19 mV (Fig. 3d inset), which compares favorably to the MTC and commercial Pt/C catalysts (a negative shift of ~50 mV for the Pt/C) as shown in Fig. S14. Meanwhile, the retention percentage of its catalytic current is 83.5% under a chronoamperometric experiment at -0.3 V during 8 hours (Fig. 3d), considerably higher than that of the Pt/C catalysts (57.8% in Fig. S14). In addition, for direct methanol fuel cells applications, the tolerance to the crossover effect is verified by the chronoamperometric measurement at -0.3 V with a rotation rate of 1,000 rpm in the O_2-saturated 0.1 M KOH solution. Immediately upon the addition of methanol, a large decrease in the catalytic current density is found for the Pt/C catalyst, while no noticeable response is observed in the MTCG catalysts under the same condition (Fig. S15), indicating that the MTCG has a high selectivity for the ORR with a remarkably good tolerance of the crossover effect.

To clarify the observed enhancement in the electrocatalytic activity of the MTC in the ORR after its intimate anchorage on the graphene sheet, we utilized unrestricted DFT calculations with the hybrid functional B3LYP based on a four-electron ORR pathway in the alkaline solution (models shown in Fig. S17).[33–35] The transition states/intermediates involved in the ORR and the energetic diagram of the catalytic reaction have been calculated, with detailed computational methods and results presented in the Computational Section of the Supporting Information. It is demonstrated that both the MTC and MTCG are capable of catalyzing the rapid reduction of O_2 to free OOH^- almost without any energetic barrier, and the re-adsorption of OOH^- is rather difficult (largely endothermic) in both cases (see **Int2 → TS2 → Int1'** in Fig. S18 and S19). Therefore, it is proposed that the electron transfer from catalysts to free OOH^- during the reduction of free OOH^- would be the rate-limiting step to account for the

difference in the catalytic efficiency between the MTC and MTCG. To test this hypothesis, additional electrons are added to the **Int2$_c$** and **Int2$_m$** intermediates (see Fig. S18 and S20 for structures), which then can be regarded as a H_2O-OOH^- complex weakly adsorbed on the surfaces of the MTC and MTCG, and re-optimized (Fig. 4). It is found that, in the MTCG system, the H_2O-OOH^- complex is decomposed into three hydroxides only when the number of added electrons is ≥ 6, while the number of additional electrons should be ≥ 7 in the case of MTC and a similar investigation reveals a number of ≥ 5 for graphene. These results imply the existence of a synergistic effect in the ORR catalyzed by the MTCG sample where graphene should take part in the reduction of free OOH^- and thus facilitate the reduction of free OOH^- and consequently the overall ORR.

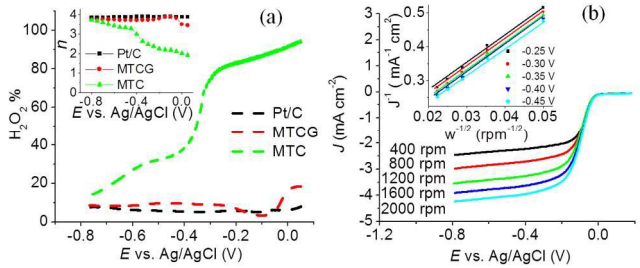

Fig. 5 (a) Peroxide percentage and electron transfer number (inset) of the MTC, MTCG and Pt/C catalysts as functions of the cathodic potential. (b) RRDE curves of the MTCG catalysts in the O_2-saturated 0.1 M KOH at different rotation rates and the inset shows the corresponding Koutecky-Levich plots at different potentials.

To verify the above proposed theoretical results, the ORR electron transfer pathway was in addition quantified by analyzing the RRDE measurements, where the amount of H_2O_2 generated at the disk electrode could be accurately determined.[36] According to Equation S1, the relative magnitudes of the ring and disk current densities determine the corresponding peroxide percentage that is plotted in Fig. 5a. The H_2O_2 yield for the MTC is strongly dependent on the applied bias, displaying a monotonic decrease of the H_2O_2 yield with the increasing cathodic potential. In the case of the MTCG, the decrease of the H_2O_2 yield is considerably faster than that of the MTC and the H_2O_2 yield is below 10% over ~90% of the whole potential range. Such an experimental result suggests the existence of a more facile pathway in reducing free OOH^- on the MTCG catalysts rather than the original MTC, as is also predicted by our theoretical calculations. It should be noted that with a mere cathodic potential of -50 mV *vs*. Ag/AgCl, the H_2O_2 yield of the MTCG well matches that of the commercial Pt/C catalyst, further demonstrating the excellence of the MTCG. Based on the ring and disk currents (Equation S3), the electron transfer number (n) is 3.71–3.90 for the MTCG and 3.84–3.90 for the Pt/C catalyst over the potential range from -0.05 to -0.8 V, and n of the MTC is found to severely deviate from 4 at low cathodic potentials (Fig. 5a inset), suggesting the sluggish reduction of OOH^- on the MTC as expected by our theoretical predictions (*vide supra*). Linear sweep voltammograms (LSVs) were also recorded from 400 to 2000 rpm (Figure 5b). An increasing current was observed with the enhanced rotation speeds for MTCG, which can be explained by the shortened diffusion distance at high speeds. In addition, n of the MTCG can also be obtained from the slope of Koutecky-Levich (K-L) plots (Equation S5). As shown in the inset of Fig. 5b, the current density measured at different potentials is proportional to the square root of the rotation speed in the LSVs due to the enhanced diffusion of electrolytes and the corresponding n is found to be 3.72 for the MTCG, in an excellent agreement with the result from Equation S3 and again confirming a predominant four-electron pathway for the oxygen reduction catalyzed by the MTCG.

4. Conclusions

In summary, we have synthesized the monoatomic-thick g-C_3N_4 dots@graphene catalysts, with an appreciably improved electrocatalytic activity rivaling that of the commercial Pt/C catalyst in the ORR. The face-to-face contact between g-C_3N_4 and graphene is believed to induce synergistic coupling interaction in facilitating the ORR and electron transport through the MTCG. The theoretical calculations and RRDE measurements indicate that the MTCG displays a higher efficiency for the reduction of OOH^- than the g-C_3N_4 alone, resulting in an enhanced performance in ORR with an efficient four-electron pathway. Rather than being confined to g-C_3N_4 and graphene systems, the current methodology of preparing ultrathin hybrid architectures is envisaged to be viable in constructing more sophisticated ultrathin heterojunctions involving other interesting 2D materials such as transition metal dichalcogenides (TiS_2, MoS_2, WSe_2, etc.), and hexagonal boron nitride for novel electrochemical applications in supercapacitors, electrocatalysis, photovoltaics and lithium ion batteries.

Table 1. Comparison of the electrocatalytic performance of MTCG in the ORR with those of previously reported g-C_3N_4-based ORR catalysts in the 0.1M KOH solution.

Loadings (μg cm^{-2})	Techniques	Potentials (V *vs*. Ag/AgCl) Peak potential (E_p) Onset potential (E_{on}) Half-wave potential ($E_{1/2}$)	Sweep rates	Samples	Sources
80.0	CV RDE RDE	E_p : -0.13 E_{on} : -0.02 $E_{1/2}$: -0.09	10 mV s^{-1} 10 mV s^{-1} 10 mV s^{-1}	MTCG	This work
70.7	CV RDE	E_p : -0.25 E_{on} : ~ -0.10 $E_{1/2}$: N/A	100 mV s^{-1} 10 mV s^{-1}	150-C/CN	Ref 13

84.8	CV RDE	E_p : -0.18 E_{on} : -0.1 $E_{1/2}$: N/A	N/A N/A	g-C_3N_4@CMK-3	Ref 20
85.0	CV RDE	E_p : -0.17 E_{on} : -0.14 $E_{1/2}$: N/A	100 mV s^{-1} 5 mV s^{-1}	G–CN800	Ref 11
283	CV RDE RDE	E_p: ~ -0.16 E_{on} : -0.054 $E_{1/2}$: -0.167	50 mV s^{-1} 5 mV s^{-1} 5 mV s^{-1}	Co-g-C_3N_4@rGO	Ref 27
283	CV RDE RDE	E_p : -0.21 E_{on} : ~ -0.08 $E_{1/2}$: ~ -0.16	50 mV s^{-1} 5 mV s^{-1} 5 mV s^{-1}	NCo-GS-0.5	Ref 28
300	CV RDE	E_p : ~ -0.21 E_{on} : -0.12 $E_{1/2}$: N/A	N/A 5 mV s^{-1}	g-C_3N_4/rGO-2	Ref 19

Acknowledgements

We thank the financial support from the 973 programs (2011CB013000 and 2011CBA00701) of China and NSFC (21103010, 21373027, 21325415, 21174019, and 51161120361), Fok Ying Tong Education Foundation (No. 131043), and the 111 Project 807012.

Notes and references

[a] *Key Laboratory of Cluster Science, Ministry of Education of China Beijing Key Laboratory of Photoelectronic/Electrophotonic Conversion Materials, School of Chemistry, Beijing Institute of Technology Beijing 100081, P. R. China. Fax: (+) 86-10-68918608 E-mail: zhipan@bit.edu.cn; shlchen@bit.edu.cn; lqu@bit.edu.cn*
[b] *Department of Chemistry, Tsinghua University Beijing 100084, P. R. China*

† Electronic Supplementary Information (ESI) available: [Computational section and full synthesis, characterization details and detailed discussions]. See DOI: 10.1039/b000000x/

1. R. F. Service, *Science,* 2009, **324**, 875.
2. Y. F. Sun, S. Gao, Y. Xie, *Chem. Soc. Rev*., 2014, **43**, 530.
3. Y. F. Sun, Z. H. Sun, S. Gao, H. Cheng, Q. H. Liu, J. Y. Piao, T. Yao, C. Z. Wu, S. L. Hu, S. Q. Wei, Y. Xie, *Nat. Commun*., 2012, **3**, 1057.
4. Y. F. Sun, H. Cheng, S. Gao, Z. H. Sun, Q. H. Liu, Q. Liu, F. C. Lei, T. Yao, J. F. He, S. Q. Wei, Y. Xie, *Angew. Chem. Int. Ed*., 2012, **51**, 8727.
5. Y. F. Sun, F. C. Lei, S. Gao, B. C. Pan, J. F. Zhou, Y. Xie, *Angew. Chem. Int. Ed*., 2013, **52**, 10569.
6. Y. F. Sun, Q. H. Liu, S. Gao, H. Cheng, F. C. Lei, Z. H. Sun, Y. Jiang, H. B. Su, S. Q. Wei, Y. Xie, *Nat. Commun*., 2013, **4**, 2899.
7. X. Wang, K. Maeda, A. Thomas, K. Takanabe, G. Xin, J. M. Carlsson, K. Domen, M. Antonietti, *Nat. Mater*., 2009, **8**, 76.
8. X. D. Zhang, X. Xie, H. Wang, J. J. Zhang, B. C. Pan, Y. Xie, *J. Am. Chem. Soc*., 2013, **135**, 18.
9. S. S. Park, S.W. Chu, C. Xue, D. Zhao, C. S. Ha, *J. Mater. Chem*., 2011, **21**, 10801.
10. M. Shalom, S. Gimenez, F. Schipper, I. Herraiz-Cardona, J. Bisquert, M. Antonietti, *Angew. Chem. Int. Ed*., 2014, **53**, 3654.
11. J. Liang, Y. Zheng, J. Chen, J. Liu, D. Hulicova-Jurcakova, M. Jaroniec, S. Z. Qiao, *Angew. Chem. Int. Ed*., 2012, **51**, 3892.
12. K. Kwon, Y. J. Sa, Jae Y. Cheon, S. H. Joo, *Langmuir*, 2012, **28**, 991.
13. S. B. Yang, X. L. Feng, X. C. Wang, K. Müllen, *Angew. Chem. Int. Ed*., 2011, **50**, 5339.
14. T. Y. Ma, S. Dai, M. Jaroniec, S. Z. Qiao, *Angew. Chem. Int. Ed*., 2014, **53**, DOI: 10.1002/anie.201403946
15. P. Niu, L. L. Zhang, G. Li, H. M. Cheng, *Adv. Funct. Mater*., 2012 **22**, 4763.
16. B. V. Lotsch, M. Doblinger, J. Sehnert, L. Seyfarth, J. Senker, O. Oeckler, W. Schnick, *Chem. Eur. J.*, 2007, **13**, 4969.
17. Z. Z. Lin, X. C. Wang, *Angew. Chem. Int. Ed*., 2013, **52**,1735.
18. V. Georgakilas, M. Otyepka, A. B. Bourlinos, V. Chandra, N. Kim, K. C. Kemp, P. Hobza, R. Zboril, K. S. Kim, *Chem. Rev*., 2012, **112**, 6156.
19. J. Q. Tian, R. Ning, Q. Liu, A. M. Asiri, A. O. Al-Youbi, X. P. Sun, *ACS Appl. Mater. Interface*s, 2014, **6**, 1011.
20. Y. Li, Y. Hu, Y. Zhao, G. Shi, L. Deng, Y. Hou, L. Qu, *Adv. Mater*., 2011, **23**, 776.
21. Y. Li, Y. Zhao, H. Cheng, Y. Hu, G. Shi, L. Dai, L. Qu, *J. Am. Chem. Soc*., 2012, **134**,15.
22. X. Xie, L. Qu, C. Zhou, Y. Li, J. Zhu, H. Bai, G. Shi, L. Dai, *ACS Nano*, 2010, **4**, 6050.
23. S. B. Yang, Y. J. Gong, J. S. Zhang, L. Zhan, L. L. Ma, Z.Y. Fang, R. Vajtai, X. C. Wang, P. M. Ajayan, *Adv. Mater*., 2013, **25**, 2452.
24. Y. Zheng, Y. Jiao, J. Chen, J. Liu, J. Liang, A. Du, W. Zhang, Z. Zhu, S. C. Smith, M. Jaroniec, G. Q. Lu, S. Z. Qiao, *J. Am. Chem. Soc*., 2011, **133**, 20116.
25. H. Darmstadt, C. Roy, S. Kaliaguine, S. J. Choi, R. Ryoo, *Carbon*, 2002, **40**, 2673.
26. A. Thomas, A. Fischer, F. Goettmann, M. Antonietti, J. Müller, R. Schlögl, J. M. Carlsson, *J. Mater. Chem.*, 2008, **18**, 4893.
27. Y. J. Cui, J. S. Zhang, G. G. Zhang, J. H. Huang, P. Liu, M. Antonietti, X. C. Wang, *J. Mater. Chem*., 2011, **21**, 13032.
28. M. T. De Groot, M. Merkx, A. H. Wonders, M. T. M. Koper, *J. Am. Chem. Soc*., 2005, **127**, 7579.
29. Y. G. Li, W. Zhou, H. L. Wang, L. M. Xie, Y. Y. Liang, F. Wei, J. C. Idrobo, S. J. Pennycook, H. J. Dai, *Nat. Nanotechnol*., 2012, **7**, 394.
30. H. T. Chung, J. H. Won, P. Zelenay, Nat. Commun., 2013, **4**, 1922.
31. Q. Liu, J. Y. Zhang, *Langmuir*., 2013, **29**, 3821.
32. J. T. Jin, X. G. Fu, Q. Liu, J. Y. Zhang, *J. Mater. Chem. A*, 2013, **1**, 10538.
33. A. D. Becke, *J. Chem. Phys*., 1993, **98**, 1372.
34. A. D. Becke, *J. Chem. Phys*., 1993, **98**, 5648.
35. C. T. Lee, W. T. Yang, R. G. Parr, *Phys. Rev. B*, 1988, **37**, 785.
36. Z. S. Wu, S. B. Yang, Y. Sun, K. Parvez, X. L. Feng, K. Müllen, *J. Am. Chem. Soc*., 2012, **134**, 9082.